International Journal of Biological Macromolecules 360 (2026) 151751

Contents lists available at ScienceDirect

International Journal of Biological Macromolecules

journal homepage: www.elsevier.com/locate/ijbiomac

A fragment of 12S seed storage protein of *Arabidopsis* forms twisted cross beta-sheet rich amyloid fibrils

Vijay Kumar [a,b], Nikolay Stoyanov [c], Vibha Kaushik [a], Sourav Kumar [a], Matthias Schmidt [c], Marcus Fändrich [c], Daniel Segal [a,d,*]

[a] Shmunis School of Biomedicine and Cancer Research, George S. Wise Faculty of Life Sciences, Tel Aviv University, Tel Aviv, 6997801, Israel
[b] School of Biosciences, Swami Rama Himalayan University, Swami Ram Nagar, Jolly Grant, Dehradun, Uttarakhand, 248016, India
[c] Institute of Protein Biochemistry, Ulm University, Ulm, 89081, Germany
[d] Sagol School of Neuroscience, Tel Aviv University, Tel Aviv, 6997801, Israel

ARTICLE INFO

Keywords:
Plant amyloids
Cruciferin-3
Amyloid structure
Cryo-EM
Biomaterials

ABSTRACT

Plant seed storage proteins (SSPs) serve as a nutrient source and are suggested to be crucial for seed survival during dormancy and desiccation. They form highly stable and environmentally stress-resistant amyloid structures. SSP amyloids are gaining significant attention for fabricating sustainable biomaterials in recent times; however, the requirement for optimized fibrillation conditions limits their practical use. Therefore, understanding the molecular mechanism of SSP amyloidogenesis, biochemical conditions, and the biophysical properties of the resultant amyloid fibrils becomes crucial. This study investigates the amyloidogenic properties of Cruciferin-3 (CRU-3), a major SSP from *Arabidopsis thaliana*, focusing on the 12-residue representative peptide, L_{223}–Y_{234} (LY12), computationally predicted to be amyloidogenic. LY12 forms β-sheet rich amyloid fibrils in a nucleation-dependent manner *in vitro* with the potential to seed self-aggregation. The peptide fibrillation was found to be pH-dependent and showed a moderate resistance to Proteinase K treatment. Molecular-level insight into the structure of LY12 fibrils was obtained using cryogenic-electron microscopy (cryo-EM) at a high resolution of 2.86 Å. The structure of LY12 fibrils revealed a C2 symmetrical, left-handed, twisted core comprising three non-equivalent peptide stacks. This unique cross β-sheet dense core, stabilized by hydrophobic and electrostatic interactions, and surrounded by low-density peptide layers, distinguishes them from pathological amyloids. This study explores the conditions for LY12 amyloid formation and deciphers their biophysical attributes and structural details, suggesting the potential physiological roles and biomaterial applications of CRU-3 amyloids.

1. Introduction

Amyloids are highly stable and well-ordered cross β-sheet rich fibrillar aggregates formed by proteins and peptides [1]. These are known to underlie the pathophysiology of various human diseases, including Alzheimer's disease (AD), Parkinson's disease (PD), and Amyotrophic lateral sclerosis (ALS) [2]. However, research in recent decades revealed that many amyloid structures perform important physiological roles and are termed as functional amyloids [3]. These amyloids are found across diverse organisms and serve various purposes, *e.g.*, they aid in bacterial biofilm formation, fungal development, yeast cell cycle regulation, and hormone storage in animals and humans [4].

Plants have long been assumed to be resistant to protein aggregation [5,6]. However, a recent *in silico* study predicted nucleic acid-binding proteins, seed storage proteins (SSPs), and defense proteins of various plant species to be potentially amyloidogenic [7]. Subsequently, the same group demonstrated that an SSP of *Pisum sativum*, 7S globulin Vicilin, possesses Cupin domains that facilitate its self-assembly to form amyloid-like structures *in vitro* and in the cotyledons. Vicilin amyloids are profoundly present during seed maturation as nutrient reservoirs that are utilized during germination [8]. Additionally, SSPs from cereals and legumes are also reported to form amyloids *in vivo* [9].

Beyond the intriguing roles of amyloids in the physiology of plant seeds, their novel application in biomaterials and food technology is

* Corresponding author at: Shmunis School of Biomedicine and Cancer Research, George S. Wise Faculty of Life Sciences, Tel Aviv University, Tel Aviv, 6997801, Israel.
E-mail address: dsegal@post.tau.ac.il (D. Segal).

https://doi.org/10.1016/j.ijbiomac.2026.151751
Received 3 October 2025; Received in revised form 15 March 2026; Accepted 30 March 2026
Available online 1 April 2026

rapidly gaining prominence [7,8]. Protein amyloid nanofibrils provide a versatile array of functional qualities to the food sector, sourced increasingly from sustainable origins, particularly plant-based proteins, such as wheat, oats, and legumes [10]. These plant amyloids possess a remarkable capacity to enhance nutrient delivery (*e.g.*, significantly improved iron bioavailability) and provide extended food preservation through intrinsic antioxidant and antimicrobial properties. Furthermore, their versatile material characteristics, such as rigidity and tensile strength for innovative texture alteration (*e.g.*, hydrogels and scaffolds for cultured meat), and intelligent packaging solutions [11,12], make them excellent alternatives in the material and food industries. Recent comprehensive *in vitro* and *in vivo* studies on engineered synthetic dietary protein amyloid fibrils, such as those derived from lysozyme and β-lactoglobulin, provide substantial evidence of their digestibility and safety [13,14].

Recent reports have proposed exploiting staple food sources, such as wheat, soy, and legumes, to meet the numerous applications of plant protein amyloids in industry and food [15,16], which might lead to a conflict between industrial demand and global food supply. Therefore, it is essential to explore strategic non-food alternatives to traditional food sources for enhanced public health, improved food security, and environmental sustainability. The protein-rich agricultural waste, such as the de-oiled cakes of oilseed crops, particularly from the Cruciferae family plants, can serve as a sustainable, high-value resource for novel biomaterials and food applications without affecting food availability or requiring additional land use [17]. *Arabidopsis thaliana* is particularly relevant in this context due to its genetic tractability as a model system for understanding fundamental protein biology and amyloid formation [18].

Cruciferins (CRUs) are the major SSPs of the Cruciferae family plants. In *Arabidopsis*, CRU is a 12S globulin and is found as three isoforms, CRU-1, CRU-2, and CRU-3, and like Vicilin, they too contain Cupin domains [19]. CRUs are mainly known to be involved in protecting the seeds from oxidative stress, thus enhancing their longevity [20]. CRU-3 stands out as it is the longest CRU isoform that has a major contribution to overall seed protein in *Arabidopsis* [21]. Moreover, it possesses unique structural characteristics, such as an extended glutamine-rich region in the center of the polypeptide and a predicted prion-like domain, that might facilitate amyloidogenesis [21,22].

In this study, we characterized the amyloidogenic nature of CRU-3 using different bioinformatic tools to predict its amyloidogenic propensity. The 12 amino acid-long peptide spanning from L_{223} to Y_{234}, thus named as LY12, was predicted to have the highest aggregation propensity and was further characterized for amyloid formation *in vitro* employing different biophysical techniques. LY12 formed amyloid fibrils through a nucleation-dependent reaction, which was accelerated by preformed LY12 fibrils, demonstrating their seeding potential. Further, we found that LY12 amyloids exhibit varying morphology at different pH ranges. The Proteinase K treatment data suggest moderate stability of LY12 amyloids against proteinase digestion. The cryogenic-electron microscopy (cryo-EM) structure showed that LY12 forms amyloid fibrils with twisted cross β-sheet topology.

We propose that CRU-3, as represented by the LY12 peptide, may form moderately stable amyloid fibrils, which might play a crucial role in seed stress management, longevity, and transition from dormancy to germination. Moreover, the seeding ability and the stability of the fibrils at a wide pH range and against enzymatic degradation make them an excellent choice for fabricating materials for different applications.

2. Materials and methods

2.1. Materials

The predicted amyloidogenic peptide LY12 ($_{223}$LVIIALLDIANY$_{234}$) of CRU-3 from *Arabidopsis thaliana* was chemically synthesized and supplied by GenScript (GenScript Biotech, Singapore). All chemical reagents and dyes were purchased from Sigma Aldrich (Rehovot, Israel) unless mentioned otherwise.

2.2. Methods

2.2.1. In silico prediction of the amyloidogenic determinants in Cruciferin-3 of Arabidopsis thaliana

The amino acid sequence of CRU-3 of *Arabidopsis thaliana* was fetched from UniProt (https://www.uniprot.org/) with accession number Q96318. It was then assessed for its aggregation potential using three widely accepted protein aggregation prediction tools, *viz.*, AmylPred2 [23] (http://thalis.biol.uoa.gr/AMYLPRED2/), FoldAmyloid [24] (http://bioinfo.protres.ru/fold-amyloid/), and pWALTZ [25] (https://waltz.switchlab.org/). The protein sequence was submitted as a query in the accepted format, and the predicted regions were identified as aggregation-prone regions (APRs).

2.2.2. Preparation of CRU-3 derived peptide for aggregation studies

The highly hydrophobic lyophilized LY12 peptide was dissolved in hexafluoroisopropanol (HFIP) to dissociate any preformed aggregates and ensure that the starting material is in a predominantly monomeric state. HFIP was then evaporated and the peptide was dissolved in 5% dimethylsulfoxide (DMSO) to prepare a 10 mM stock solution. DMSO is a widely used solvent for amyloid studies, and at concentrations as low as 5%, it does not interfere with amyloidogenesis. The peptide was then diluted to different concentrations (10 μM, 25 μM, 50 μM, 100 μM, and 200 μM) in PBS (pH 7.4) and incubated at 37 °C for 72 h, rotating at 500 RPM on a thermoshaker (MRC Lab, Holon, Israel) for the initial 12 h, and then in static mode.

2.2.3. Thioflavin-T binding and aggregation kinetics

Initially, the LY12 aggregates were assessed for amyloid formation by monitoring their Thioflavin-T (ThT) binding. The aggregated samples at different concentrations (10 μM, 25 μM, 50 μM, 100 μM, and 200 μM) were transferred to a black 96-well plate (Corning, New York, USA), and 20 μM ThT, prepared in PBS (pH 7.4), was added to the samples. The plate was incubated for 10 min at room temperature (RT), and the ThT fluorescence intensity was then recorded on an Infinite M200 PRO microplate reader (Tecan, Männedorf, Switzerland) at 485 nm after exciting the dye at 440 nm. The ThT alone served as a control.

Further, the aggregation kinetics of the LY12 peptide was assessed at different concentrations. For this purpose, the peptide samples diluted at the above-mentioned concentrations were incubated with 20 μM ThT in a black 96-well plate at 37 °C and 45 °C, and the fluorescence intensity was recorded at 485 nm by exciting ThT at 440 nm at an interval of 5 min for 90 h. The samples were shaken at 280 RPM for 1 min before each reading.

2.2.4. Congo red spectral shift assay

LY12 aggregates formed at different concentrations were mixed with 35 μM Congo red (CR) in a transparent flat-bottom 96-well plate. The samples were incubated for 15 min at RT, and the CR absorption spectra were recorded from 400 nm to 700 nm on an Infinite M200 PRO microplate reader. The CR alone served as a control.

2.2.5. Circular dichroism spectroscopy

Since DMSO is incompatible with circular dichroism (CD), LY12 was dissolved in HFIP to make a 10 mM stock solution. To track the amyloid-specific structural transitions, the LY12 solution was diluted to 200 μM in 10 mM sodium phosphate buffer (pH 7.4). The peptide solution was then transferred to a 0.1 cm quartz cuvette. Thereafter, the CD spectrum was recorded from 190 nm to 260 nm on a Chirascan spectropolarimeter (Applied Photophysics, UK) at 25 °C. After recording the spectrum, the sample was recollected and incubated for amyloid formation for 72 h as mentioned earlier. After incubation, the sample was scanned again using the same parameters. The buffer devoid of the peptide was taken as a

blank for baseline correction.

2.2.6. Transmission electron microscopy

A 5 μL aliquot of the aggregated LY12 at an initial concentration of 200 μM was drop-cast onto a Formvar-coated 400-mesh copper grid (Ted Pella, Inc., USA). The aggregates were allowed to bind for 40 s on the grid surface. The excess sample was removed using a lint-free tissue. Then, the grid was negatively stained by loading 5 μL of an aqueous solution of 2% (w/v) phosphotungstic acid on the grid. The excess staining solution was removed with a lint-free tissue. The grid was air-dried overnight and then observed under a JEM-1400Plus transmission electron microscope (TEM) (JEOL, Tokyo, Japan) accelerating at 80 kV.

2.2.7. Assessment of the effect of different pHs on LY12 amyloid formation

LY12 was diluted to a final concentration of 50 μM in buffers of different pHs (2, 4, 6, 7.4, and 9) with 20 μM ThT in a black 96-well plate. Subsequently, the aggregation of the peptide at different pHs was monitored by recording the ThT fluorescence intensity over a period of 72 h as mentioned above. The readings of the ThT controls at different pHs were subtracted from the respective test samples during data analysis. We performed TEM analysis as explained above to observe the morphology of the resultant aggregates under different pH conditions.

2.2.8. Assessment of the proteinase stability of LY12 amyloid fibrils

The amyloids formed at a concentration of 200 μM were diluted in 20 μL of 200 mM Tris buffer (pH 8.0), containing 1.4 M NaCl and 20 mM $CaCl_2$. Then, 1.38 mM Proteinase K and 20 μM ThT were added to the diluted amyloids. The sample was transferred to a black 96-well plate, and the ThT fluorescence intensity was recorded every 30 min for 12 h at 37 °C. At the end of the treatment, Proteinase K activity was stopped by adding 0.5 μL of 200 mM phenylmethylsulfonyl fluoride (PMSF) and incubating for 10 min at RT. Untreated LY12 amyloids mixed with ThT were treated as the negative control. The corresponding fluorescence intensity of the ThT control was subtracted from those of both treated and untreated samples. The morphology of the untreated and treated amyloids was visualized by TEM imaging as described above.

2.2.9. Investigation of the seeding potential of LY12 amyloids

As mentioned above, the LY12 amyloid fibrils were prepared by incubating 200 μM of the peptide. Subsequently, the preformed fibrils were diluted to 50 μM in PBS (pH 7.4), and the diluted fibrils were then vortexed for 30 s and then sonicated for 3 min. This cycle of alternate vortexing and sonication was repeated three times to break the fibrils. The resultant solution was considered as seeds. Afterward, a freshly prepared solution of 50 μM LY12 peptide (considered monomeric) was spiked with 5% (w/w) and 10% (w/w) of the seeds in a final volume of 200 μL. The samples were then mixed with 20 μM ThT in a black 96-well plate. The aggregation reactions of the unseeded and seeded samples were monitored by recording the ThT fluorescence at 485 nm for 50 h at an interval of 60 min at 37 °C.

2.2.10. Cryogenic-electron microscopy

Aliquots of 3.5 μL of the fibril solution were applied to glow-discharged (PELCO easiGlow™, Ted Pella, Inc., USA) holey carbon-coated grids (Protochips, USA). The grids were incubated with the fibril solution for 30 s using a chamber humidity of 95%, after which they were blotted for 8 s and plunge frozen into liquid ethane using an EM GP2 plunge freezer (Leica Microsystems GmbH, Germany). Initial screening of the prepared grids was performed on a JEM-2100 TEM (JEOL, Tokyo, Japan). Data for the reconstruction was obtained on a Titan Krios cryo-EM (Thermo Fisher Scientific, USA) with an acceleration voltage of 300 kV, equipped with a Falcon 4 camera (Thermo Fisher Scientific, USA) and a Selectris X 10 eV imaging filter (Thermo Fisher Scientific, USA). The specific data acquisition parameters are mentioned in Table S1.

2.2.11. Helical reconstruction

Helical reconstruction was performed in RELION 5.0-beta [26]. Contrast transfer function estimation and motion correction of the obtained frames were performed using CTFFIND-4.1 [27] and RELION's implementation of MotionCor2 [28], respectively. A statistical estimation of the distribution of fibril morphologies was performed using 4× binned images. The different morphologies were manually picked, separately. 177,736 helical segments were extracted with box sizes varying from 200 to 420 Å. Reference-free two-dimensional (2D) classification was performed for twenty iterations with $T = 2$ and the expectation-minimization algorithm. All particles were used for three-dimensional (3D) classification with a featureless cylinder as a reference. For the 3D classification, four classes were used for twenty iterations with $T = 4$ and blush regularization [29]. The 3D classification was performed iteratively with the best class as a reference and discarding bad quality particles (42,777) until no further improvement was observed. During 3D classification and 3D auto refinement, the enforcement of C1, C2, and pseudo-2_1 screw symmetries was explored. Only a C2 helical symmetry allowed us to achieve a high-resolution reconstruction, which was in agreement with the obtained 2D class averages. After multiple rounds of classification and auto-refinement, helical segments were passed through Bayesian polishing and CTF refinement in RELION. The final auto-refinement was performed with 134,959 polished particles, after which the density map was processed with a wide mask and sharpened with an automatically determined B-factor in RELION. The final resolution of 2.86 Å was calculated using gold-standard corrected Fourier Shell Correlation (FSC) in cryoSPARC [30].

2.2.12. Model building

Three straight poly-L-alanine chains were created *de novo* in UCSF ChimeraX [31] and placed into the density. Their backbones were adjusted to fit the center of the density in Coot [32]. The side chains were gradually replaced to yield the sequence of the peptide. During modeling in Coot, non-crystallographic symmetry restraints, Ramachandran restraints, and planar peptide restraints were used. After achieving a satisfactory fit of the chains, C2 and helical symmetries were applied sequentially with the pdbsymm program from the Situs package [33]. The model was then validated using Phenix [34] and optimized for clash-score, Ramachandran distribution, rotamer and geometry quality. One half-layer was extracted, re-refined, and extended to a six-layer stack, which was subjected again to refinement. This cycle was repeated until a satisfactory fit of the model to the density was achieved with no clashes, rotamers, Ramachandran and geometry outliers. For parts of the process, ISOLDE [35] was used to minimize clashes between hydrophobic side chains along the z-axis. The details and composition of the obtained model are summarized in Table S2.

2.2.13. Isolation of protein bodies from Arabidopsis thaliana seeds

Protein bodies from the seeds of *Arabidopsis thaliana* were isolated according to the protocol described in [36] with some modifications. Briefly, mature seeds (1–2 g) of *Arabidopsis thaliana* (Columbia ecotype) were harvested and homogenized in 20 mL glycerol using a mortar and a pestle. The homogenate was filtered through four layers of muslin cloth and centrifuged for 10 min at 3000 RPM. To collect protein storage vacuoles (PSVs), the supernatant was centrifuged for 30 min at 40,000 RPM in a thick-wall polyallomer tube using a Beckman Coulter Ti 70.1 rotor. The pellet was resuspended in 20 mL of 100% (v/v) glycerol and centrifuged for 30 min at 41,000 RPM. The pellet obtained at this step contained the PSV fraction and was further suspended in 5 mL Tris-EDTA buffer (1 mM EDTA, 5 mM Tris-HCl; pH 8.5) to disrupt the PSVs. The sample was then loaded onto a discontinuous sucrose density gradient (30%, 45%, and 68% (w/v) sucrose in Tris-EDTA buffer) and centrifuged for 2 h at 41,000 RPM. The fraction in between the 45% and 68% sucrose layer represents the protein bodies containing the storage proteins. The presence of the SSPs in the isolated sample was examined

by running it on a denaturing polyacrylamide gel. The amyloidogenic characteristics of this material were subsequently examined by fluorescence microscopy.

2.2.14. Fluorescence imaging of protein bodies

The isolated protein bodies were stained with 20 μM ThT for 15–20 min at RT. The stained isolate was then drop-cast on a glass slide and covered using a coverslip. The slide was kept in the dark for drying at RT. The unstained isolate was also processed in the same way and taken as a control to distinguish the intrinsic fluorescence of the isolated seed material from that of ThT. The images were then obtained by exciting ThT with a 458 nm argon laser on an LSM 510 META confocal laser scanning microscope (Zeiss, Germany) with EC Plan-Neofluar 10× objective at 10× magnification, and a numerical aperture of 0.3.

3. Results

3.1. Cruciferin-3 possesses an intrinsic amyloidogenic propensity

We first investigated the intrinsic amyloidogenicity of CRU-3 by using AmylPred2, FoldAmyloid, and pWALTZ. These machine learning-based tools predict APRs in a protein sequence. Fig. 1 shows the APRs predicted by different *in silico* methods. AmylPred2 identified eleven amyloidogenic fragments (C_{70}–E_{81}, L_{85}–S_{93}, K_{95}–G_{104}, P_{222}–A_{232}, A_{274}–L_{287}, V_{367}–L_{372}, I_{374}–L_{380}, E_{403}–C_{407}, G_{432}–I_{437}, Q_{439}–S_{447}, and F_{452}–S_{456}). FoldAmyloid predicted ten such regions of different lengths (E_{59}–H_{63}, A_{76}–I_{80}, L_{85}–T_{92}, L_{223}–D_{230}, R_{243}–L_{247}, N_{267}–G_{271}, L_{372}–L_{380}, F_{441}–Q_{446}, F_{452}–F_{457}, and S_{473}–L_{478}). pWALTZ highlighted six regions (A_{212}–G_{219}, P_{222}–Q_{235}, N_{402}–C_{407}, Q_{439}–V_{445}, K_{451}–F_{457}, and Q_{514}–A_{524}) to be prone to form amyloids. Collectively, among the sixteen predicted amyloidogenic fragments, three, four, and two regions were identified uniquely by AmylPred2, FoldAmyloid, and pWALTZ, respectively. Four of the APRs were identified by both AmylPred2 and FoldAmyloid, and one segment was predicted by AmylPred2 and pWALTZ together. Three regions (L_{223}–D_{230}, F_{441}–V_{445}, and F_{452}–S_{456}) were predicted as APRs by all the programs. Out of these, L_{223}–D_{230} is the longest; thus, we selected it for the *in vitro* analysis. When chemically synthesizing, we extended it on the C-terminus by four amino acids (I_{231}–Y_{234}), which were predicted to be amyloidogenic by AmylPred2 and pWALTZ. Moreover, due to the presence of an aromatic amino acid (Y_{234}), this extension facilitated the spectroscopic quantification of the peptide concentration at 280 nm. We named the resultant APR peptide (L_{223}–Y_{234}) as LY12 that served as a proxy for the kinetic and structural characterization of CRU-3.

3.2. The Cruciferin-3-derived aggregation-prone region (LY12) self-assembles into amyloid-like fibrils in vitro

We asked whether the peptide, LY12, computationally predicted as amyloidogenic, forms amyloids *in vitro*. To that end, the LY12 peptide was incubated at different concentrations (10 μM, 25 μM, 50 μM, 100 μM, and 200 μM) in PBS (pH 7.4) at 37 °C on a thermoshaker for 72 h, rotating at 500 RPM for the first 12 h and continuing in static mode thereafter.

We first performed a ThT binding assay. ThT is a commonly used amyloid reporter dye that emits high fluorescence upon binding with β-sheet fibrils [37]. The incubated peptide was mixed with 20 μM ThT and transferred into a black 96-well plate to record the ThT fluorescence intensity. We observed a remarkable enhancement in ThT-specific fluorescence in a concentration-dependent manner compared to the ThT control (Fig. 2a), demonstrating amyloid-like self-assembly of the aggregates.

To further validate LY12 amyloid formation, a CR spectral shift assay was performed. CR exhibits affinity toward the cross β-sheets of amyloid fibrils, and the binding leads to a sharp red shift in the absorption maximum (480 nm) of the dye [38]. Fig. 2b shows shifts of 16 nm, 18 nm, and 20 nm for 50 μM, 100 μM, and 200 μM of LY12 aggregates, respectively, while at lower concentrations, 10 μM and 25 μM, LY12 assemblies exhibited shifts of 8 nm and 12 nm, respectively. The concentration-dependent red shifts in CR absorption maximum corroborates the finding of the ThT binding assay, suggesting the formation of

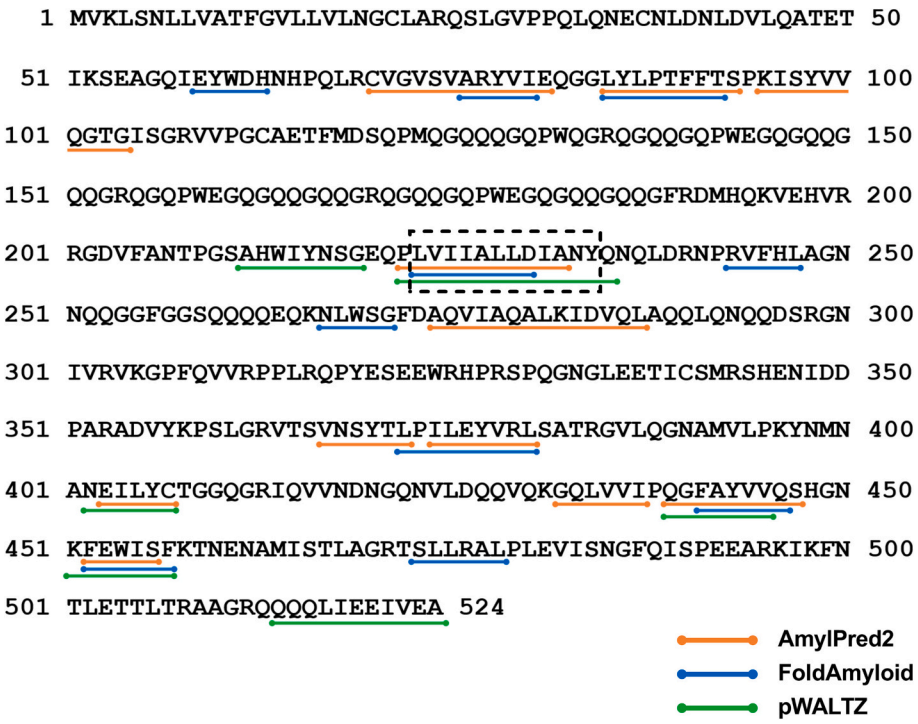

Fig. 1. *In silico* analysis of the amyloidogenic propensity in CRU-3 of *Arabidopsis thaliana*. The prediction tools, AmylPred2 (orange), FoldAmyloid (blue), and pWALTZ (green) predicted APRs in the primary structure of CRU-3 (UniProt ID: Q96318). The region LY12 ($_{223}$LVIIALLDIANY$_{234}$), shown in a dashed box, is commonly predicted by all the tools.

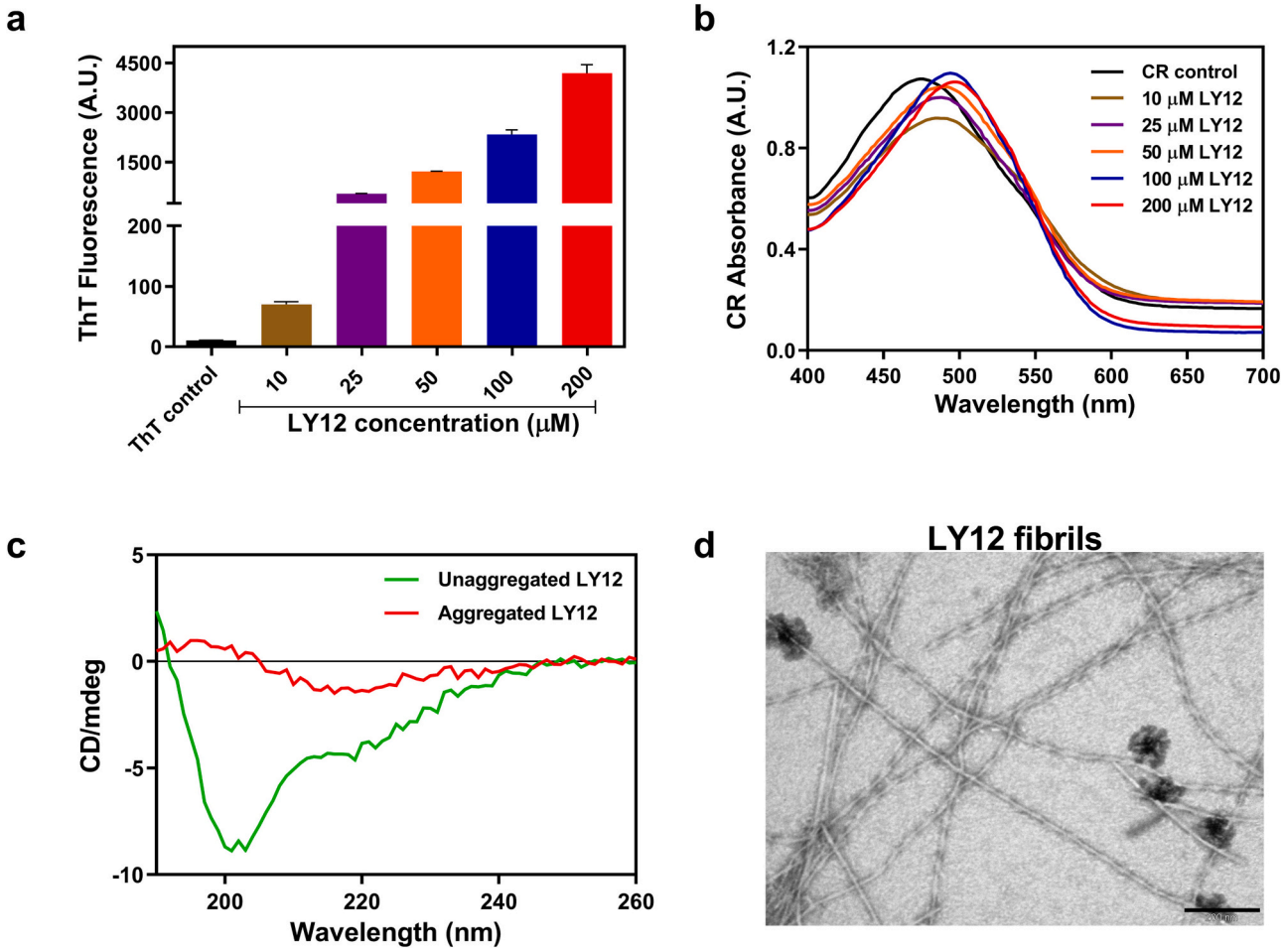

Fig. 2. *In vitro* characterization of LY12 amyloids. (a) The bar graph indicates concentration-dependent amyloid formation by LY12 as shown by increasing ThT fluorescence intensity at 485 nm with increasing LY12 concentration. The ThT alone served as a control. The error bars represent the standard deviation ($n = 3$). (b) The spectra show increasing bathochromic shifts in the CR absorption with the rise in LY12 peptide concentration compared to the CR control. (c) The CD spectra display the secondary structural alterations and formation of β-sheets in LY12 (200 μM) upon aggregation. (d) The transmission electron micrograph depicts the fibrillar morphology of LY12 aggregates formed at a concentration of 200 μM. The scale bar corresponds to 200 nm.

cross β-sheet rich assemblies upon incubation.

We then confirmed the β-sheet formation by performing CD analysis. A negative ellipticity peak at 202 nm was recorded in the CD spectrum of the unincubated LY12 peptide, reflecting the random coil structure of the monomers (Fig. 2c). The CD spectrum of LY12 after 72 h of incubation exhibited a negative ellipticity band at 220 nm and a positive CD signal at 195 nm, which corresponds to β-sheets, signifying the formation of amyloids.

Next, the morphology of the resultant LY12 amyloids was assessed by visualizing them under a TEM. As shown in Fig. 2d, the aggregated LY12 peptide formed characteristic long, unbranched amyloid fibrils with a twisted morphology.

3.3. LY12 shows a concentration-dependent aggregation kinetics

We next followed the kinetics of the LY12 amyloid formation by

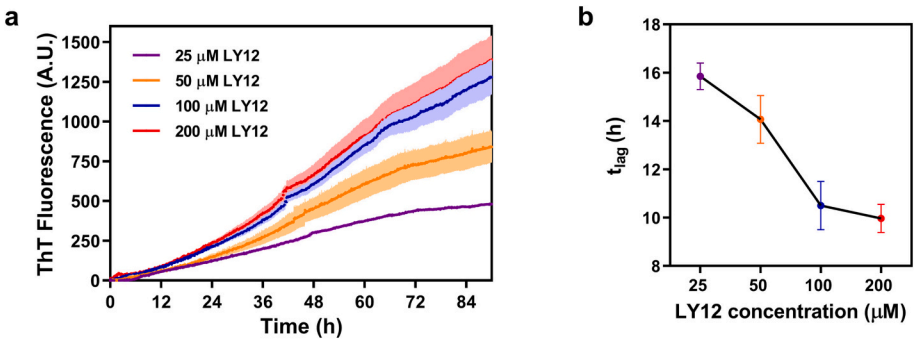

Fig. 3. The aggregation kinetics of LY12 at different concentrations. (a) The aggregation reaction of LY12 at pH 7.4, tracked by ThT fluorescence at 485 nm at regular intervals of time, shows that the rate of its aggregation accelerates with increasing initial concentration. (b) The graph of the time taken for the nucleation event (t_{lag}) against LY12 concentrations shows that the lag time reduces as the concentration increases. The error bars exhibit the standard deviation of triplicate measurements.

recording the ThT fluorescence intensity of the peptide, incubated at four different concentrations (25 μM, 50 μM, 100 μM, and 200 μM), every 5 min for 90 h. Fig. 3a shows aggregation kinetics with three distinct growth phases; the lag, the logarithmic, and the stationary phase, indicating that the LY12 aggregation process is nucleation-dependent. The lag time 't_{lag}' (time point at which the ThT signal reached 5% of the maximal amplitude achieved under the experimental time frame), shown in Fig. 3b, is 15.85 ± 0.55 h, 14.06 ± 0.98 h, 10.5 ± 0.99 h, and 9.96 ± 0.57 h for 25 μM, 50 μM, 100 μM, and 200 μM LY12, respectively. The reduction in t_{lag} with the increasing peptide concentration suggests the aggregation reaction to be concentration-dependent. The concentration-mediated acceleration in the nucleation process shows the similarity of LY12 with model amyloidogenic peptides, such as islet amyloid polypeptide (IAPP) and amyloid beta (Aβ42) [39,40].

Additionally, we performed the LY12 kinetic studies at 45 °C to confirm that the LY12 amyloidogenesis remains intact at higher temperatures. However, we observed a lower ThT intensity compared to that observed at 37 °C with a similar kinetic profile (Fig. S1), which was in agreement with a previous study [8]. This suggests that while the amyloidogenic pattern remains the same, 37 °C provides the optimal balance for high-resolution characterization of the concentration-dependent kinetics; therefore, we chose this temperature point for further experimentation and consistency.

3.4. The self-assembly process and morphology of the resultant LY12 aggregates are affected by varying pH conditions

Studying the effect of different pH environments on amyloid formation is crucial for elucidating the amyloidogenic potential and establishing optimal industrial processing parameters for proteins. Previously, amyloid formation from various seed proteins has been induced at acidic pH combined with high temperature (85–95 °C) [41,42]. Therefore, we examined the kinetics of LY12 amyloid formation at various pHs (2, 4, 6, 7.4, and 9) for 72 h using the ThT binding assay. LY12, at acidic pH of 2 and 4, exhibited a flat kinetic curve throughout the incubation time with no apparent growth phases (Fig. 4a). However, at pH 6, it exhibited a marked increase in ThT fluorescence with a lag phase of ~12 h, indicating amyloid formation. The pH 7.4 and pH 9 were found to be more favorable for amyloidogenesis, as the lag time further dropped to ~6 h and ~2 h, respectively. The lower aggregation tendency at acidic pH might be due to a change in the overall charge of the peptide and its increased solubility.

TEM analysis of the self-assemblies at the end of the aggregation reaction revealed heterogeneous structures formed by LY12 when incubated at different pHs (Fig. 4b–f). At low pH of 2 and 4 (Fig. 4b and c), LY12 formed large clumps of non-fibrillar amorphous aggregates. The amyloid fibrillar population started appearing at pH 6 (Fig. 4d) and became abundant with increasing pH, *i.e.*, 7.4 and 9 (Fig. 4e and f). The appearance of non-fibrillar structures at low pHs correlates with the ThT kinetics, where the peptide did not follow a typical sigmoidal growth curve at acidic pHs.

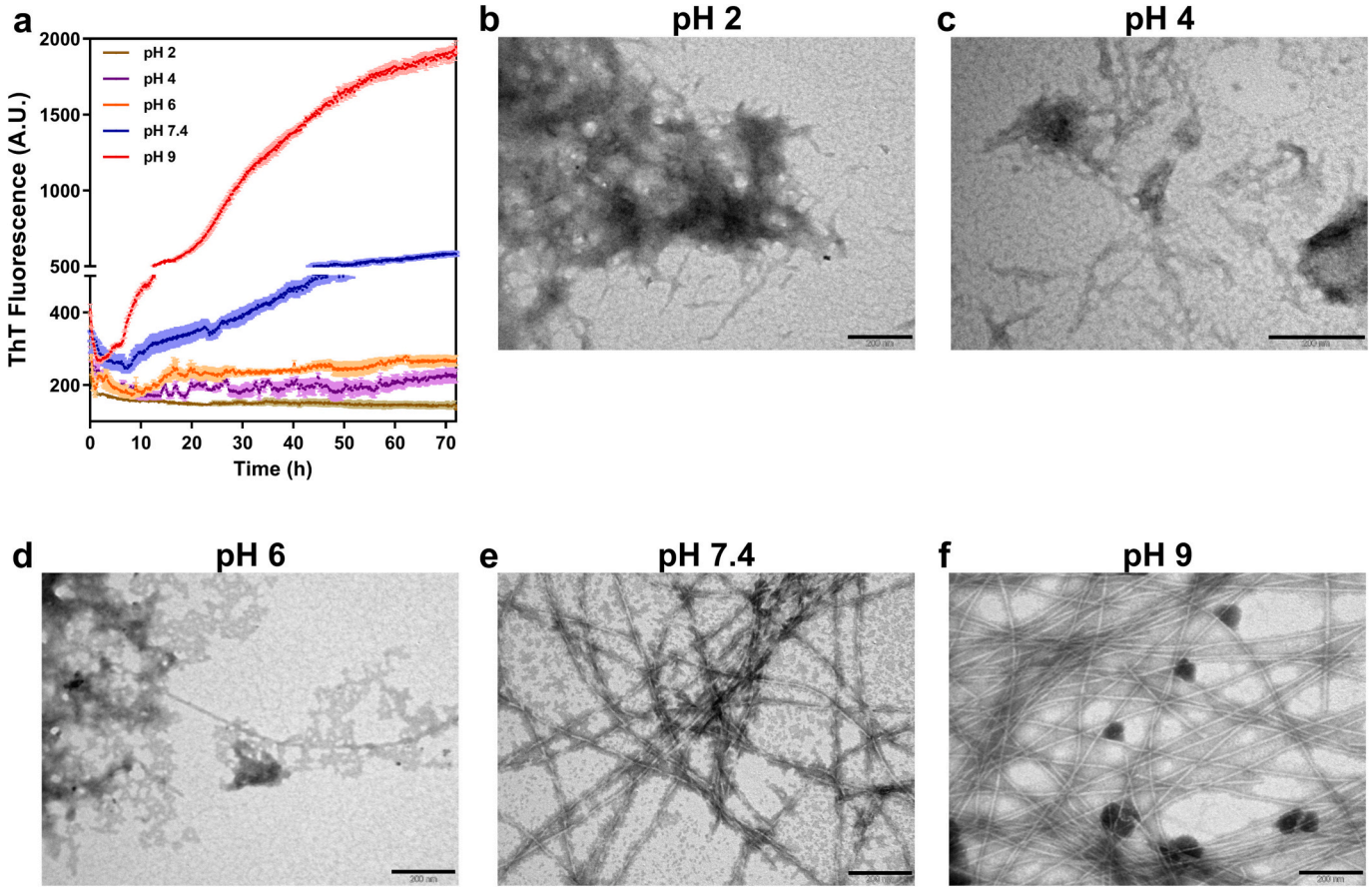

Fig. 4. The effect of pH on LY 12 amyloid formation. (a) The ThT fluorescence at 485 nm against time at different pHs (2, 4, 6, 7.4, and 9) shows pH dependence of the rate of aggregation of LY12 (200 μM). The corresponding ThT control readings were subtracted. The error bars represent the standard deviation of triplicate measurements. (b–f) The transmission electron micrographs at (b) pH 2, (c) pH 4, (d) pH 6, (e) pH 7.4, and (f) pH 9 denote diverse morphologies of LY12 aggregates formed at different pHs. The scale bar corresponds to 200 nm.

3.5. The LY12 aggregates exhibit moderate resistance to proteinase degradation

Amyloids are known to be exceptionally resistant to denaturation and proteolysis [43]. The proteolytic stability of the LY12 fibrils formed at pH 7.4 was assessed by treating them with Proteinase K and monitoring the changes in the ThT intensity over a period of 12 h. The untreated fibrils served as a control. As shown in Fig. 5a, a gradual decline in fluorescence intensity was observed in treated samples compared with untreated controls; however, the reduction was only partial. At 12 h, Proteinase K-treated fibrils retained ~38% of their initial fluorescence, representing a ~2.6-fold lower signal relative to untreated fibrils. This substantial decline in the ThT intensity suggests proteolytic degradation of the accessible fibrillar regions instead of complete digestion. This exclusive reduction of the ThT signal arose from enzymatic activity rather than spontaneous disassembly, as a similar effect was not observed in the untreated LY12 amyloids.

Transmission electron microscopy supported this interpretation, wherein Proteinase K-treated fibrils appeared shorter and more fragmented yet retained amyloid-like morphology (Fig. 5b), whereas untreated LY12 fibrils persisted as dense, elongated filamentous networks (Fig. 5c). These results demonstrate that LY12 fibrils exhibit moderate stability against proteolysis, with partial susceptibility even after a prolonged enzymatic treatment of 12 h, reflecting a compact amyloid core protected from enzymatic attack, which is a signature feature of functional amyloids [44–46].

3.6. LY12 amyloids possess the potential to seed and accelerate self-assembly

Amyloid fibrils can catalyze the aggregation of monomers into fibrils by reducing the lag phase through a phenomenon called seeding [47]. In a seeding event, preformed amyloids of a protein can act as a seed and catalyze the aggregation by accelerating the nucleation event [48]. To examine the seeding ability of LY12 amyloid fibrils, the preformed LY12 fibrils were diluted to 50 μM and fragmented to produce seeds. Thereafter, LY12 monomers (50 μM) were spiked with the seeds equivalent to 5% and 10% (w/w) of the monomeric peptide. The fibrillation kinetics was followed by adding 20 μM ThT and recording the fluorescence at an interval of 60 min for 50 h. Fig. 6 shows the seeding effect of preformed LY12 amyloids on the aggregation kinetics, wherein the lag phase (measured in terms of t_{lag}) of the unseeded reaction of 8 ± 2 h was reduced to 3.16 ± 0.57 h when subjected to 5% seeds and further reduced to 2.66 ± 1.04 h when 10% seeds were used. This catalytic efficiency of the LY12 amyloids suggests their similarity to the canonical amyloid peptides and proteins [49,50].

3.7. Cryo-EM reveals the ordered core structure of the LY12 fibrils

Analysis of LY12 fibrils with cryo-EM shows the presence of multiple fibril morphologies (Fig. 7a). The main fibril morphology possessed regularly spaced crossovers that occurred at a distance of 47 ± 7.6 nm ($n = 50$). The fibril width was measured to be 10 ± 1.3 nm ($n = 50$). In accordance with the recorded micrographs, we reconstructed the 3D map of this fibril morphology at a resolution of 2.86 Å (Table S1, Fig. S2a and b), based on the 0.143 FSC criterion (Fig. S2c and d). The fibril was found to be C2 symmetrical and showed a left-handed, twisted topology as confirmed with platinum side shadowing (Fig. S3). The fibril 3D map was relatively well-defined at inner radial positions (Fig. S2d). The well-defined region was fitted with a molecular model, and we hereafter refer to this part of the fibril structure as the fibril core (Fig. 7b and c). Attempts to reconstruct the other fibril morphologies resulted in 3D maps of lower resolutions that could not be interpreted with a reliable molecular model.

Based on the modeling of the main fibril morphology, we found the fibril core to contain three non-equivalent peptide stacks, designated here as A, B, and C (Fig. 7b and c). The peptides from stacks B and C could be traced from residue L_{223} to Y_{234}, while those in stack A could be traced from residue L_{223} to A_{232}, indicating that some residues are conformationally disordered. The peptides from stacks A and C exhibited relatively straight conformations, while those from stack B were kinked between residues A_{227} and L_{229} (Fig. 8a). The peptides of all the stacks were significantly β-sheet rich and participated in the formation of parallel cross β-sheets (Fig. 8b), although there were differences concerning the residues forming the fibril cross β-structure in different peptide stacks (Fig. 8c). The well-defined fibril core was decorated with peripheral density features of lower resolution (Fig. 7b), suggesting the attachment of additional layers of peptides at outer radial positions. Similar observations were made previously with catalytic peptide fibrils [51].

The fibril structure was stabilized by hydrophobic interactions between adjacent peptide stacks. Examples are the interfaces between stacks A (involved residues: I_{225}, A_{227}, L_{229}, I_{231}) and B (involved residues: L_{223}, I_{225}, A_{227}, L_{228}), and the contact site between the peptides in stacks B (involved residues: V_{224}, I_{226}, L_{229}, I_{231}) and C (involved residues: L_{228}, I_{226}, V_{224}) (Fig. 8d). In addition, we noted that the peptides were aligned such that there were pairings of chemical groups with opposing charges, suggesting the formation of electrostatic interactions. These pairings occurred, *e.g.*, between the N-terminal α-amino groups of the peptides in stack C and the α-carboxyl groups of the peptides in stack B. Another pairing occurred between the N-terminal α-amino groups of the peptides in stack B and the D_{230} side chain carboxyl groups of the peptides in stack C (Fig. 8d).

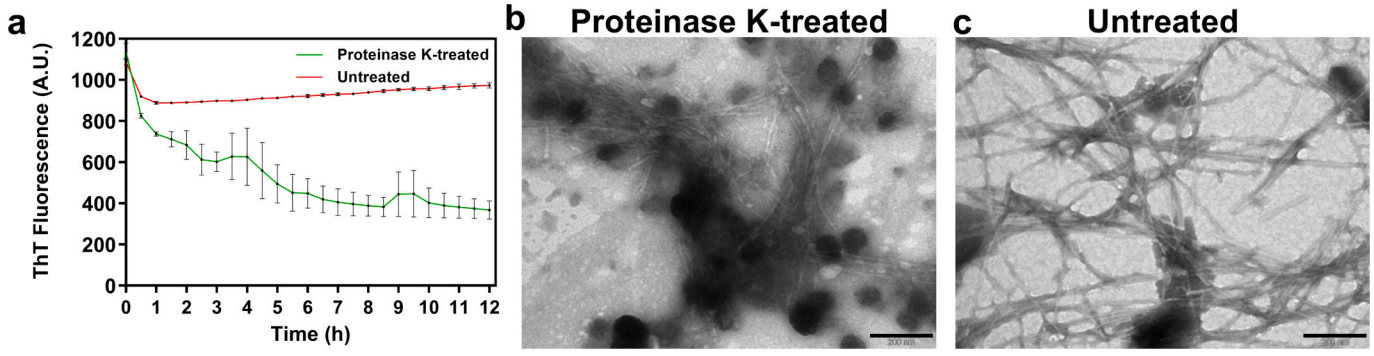

Fig. 5. The impact of Proteinase K on LY12 amyloids. (a) The LY12 amyloids, upon treatment with Proteinase K over 12 h, exhibit a gradual decline but retain ~38% of ThT fluorescence compared to the untreated amyloids, signifying moderate proteinase-resistance of these assemblies. The corresponding ThT control readings were subtracted. The error bars show the standard deviation of triplicate measurements. (b, c) The transmission electron microscopic images of (b) Proteinase K-treated LY12 amyloids show shorter, fragmented, and less abundant fibrils as compared to (c) the untreated amyloids. The scale bar is 200 nm.

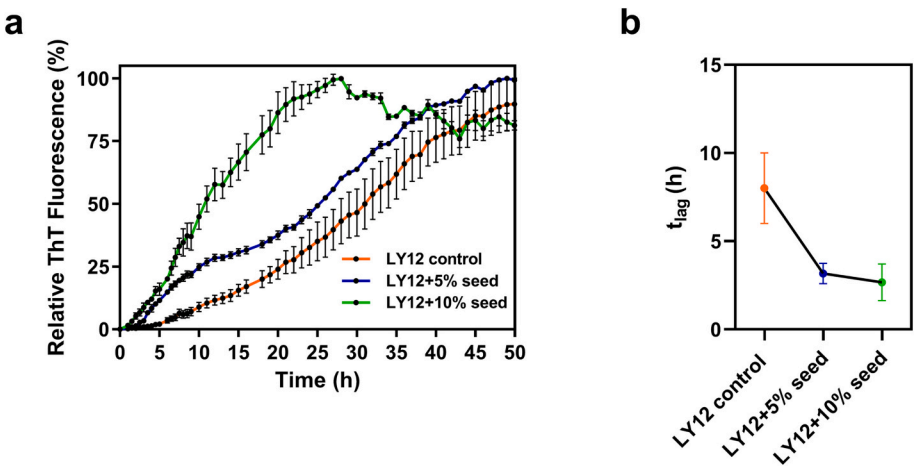

Fig. 6. Analysis of the seeding effect of LY12 amyloids. (a) The relative ThT fluorescence of the aggregation reaction over 50 h recorded at 485 nm shows accelerated LY12 aggregation when seeded with 5% and 10% preformed LY12 amyloids as compared to that of the unseeded LY12 peptide. The corresponding ThT control readings were subtracted. (b) The nucleation period (t_{lag}) reduced with increasing seed concentration. The error bars show the standard deviation of triplicate measurements.

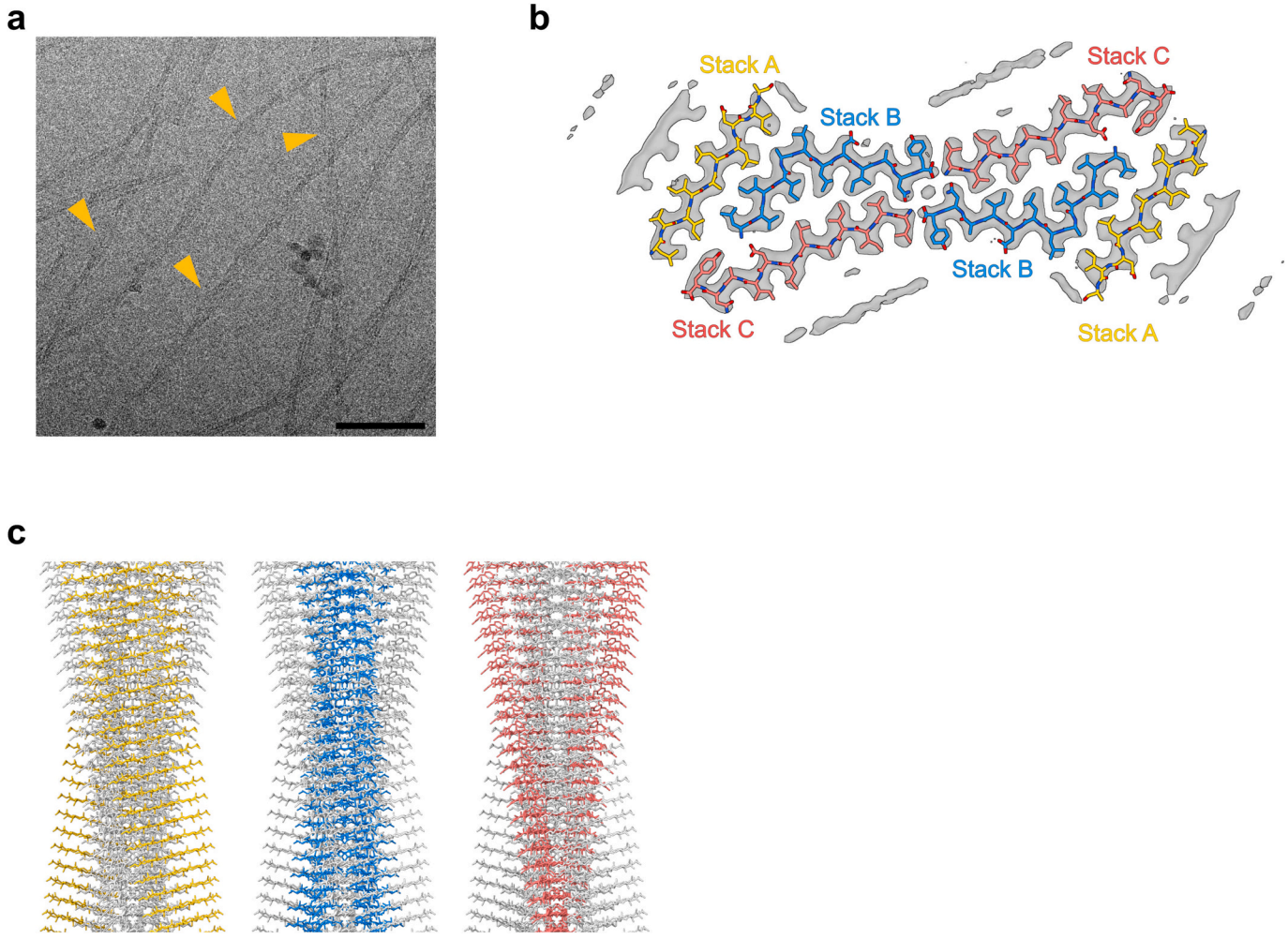

Fig. 7. Cryo-EM analysis of LY12 fibrils. (a) A raw cryo-electron micrograph showing fibrillar morphology of LY12 aggregates. The yellow arrowheads indicate the main morphology. The scale bar corresponds to 500 nm. (b) A cross-sectional view of one molecular layer of the 3D map (grey) superimposed with the molecular model of the peptides in stacks 'A' (yellow), 'B' (blue) and 'C' (red). (c) Side views of the molecular models highlighting the peptides in the different stacks.

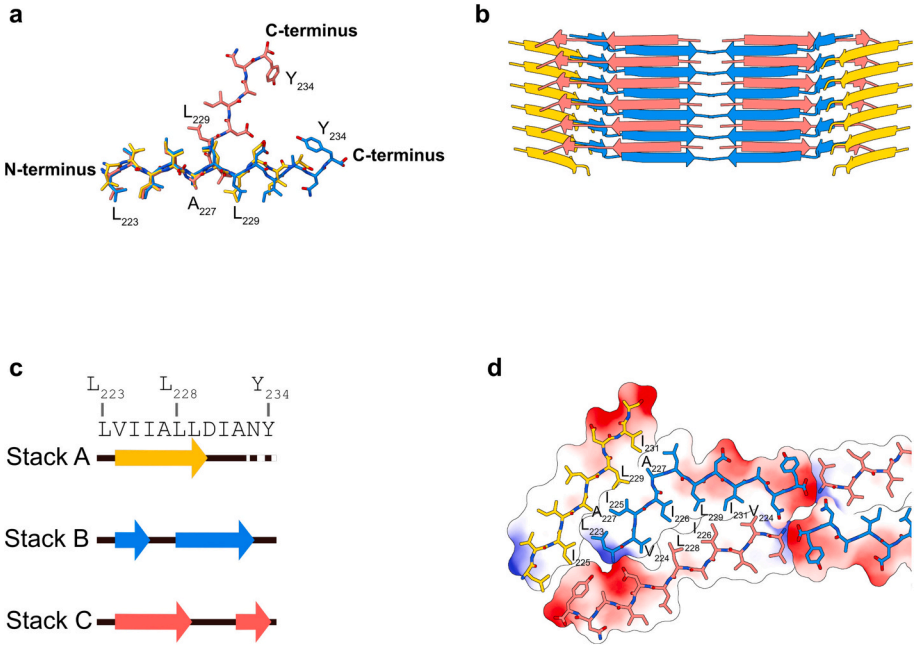

Fig. 8. Structure of the peptide stacks in the fibril core. (a) An overlay of the peptides from stacks 'A' (yellow), 'B' (blue) and 'C' (red). The peptides are aligned at the first four residues. (b) A side view of a z-axial segment of the fibril containing six molecular layers. (c) The location of β-strands (arrows) in the sequence of the LY12 peptide. The dots refer to the residues (N_{233} and Y_{234}) in stack A, which are not seen in the 3D map. (d) An overlay of peptides in one cross-sectional layer and the hydrophobicity map plotted onto a surface model of the peptides, showing that the peptides interact with each other mainly by hydrophobic contacts.

3.8. The protein bodies of Arabidopsis thaliana contain amyloid aggregates

Seed protein bodies are a hub of SSPs, with CRUs being their major constituents in *Arabidopsis* plants, accounting for more than 70% of the total proteins [52]. After studying CRU-3 amyloidogenesis *in vitro* using LY12 as its representative peptide, we sought to identify if similar structures are present in *Arabidopsis* seed protein bodies. Therefore, we isolated the protein bodies from mature *Arabidopsis thaliana* seeds by density gradient centrifugation, and the isolated material was loaded onto an SDS gel (Fig. S4a) to monitor the presence of the CRUs. The CRUs are 12S globular proteins that migrate as an α chain (35 kDa) and a β chain (25 kDa) on SDS-PAGE. The gel migration pattern matched the published data for the migration of CRUs [21]. In addition to the presumed 12S CRU polypeptide chains, the isolated protein bodies also contained 2S Albumin, which we hypothesize to be sequestered by the CRU-3 aggregates in the protein bodies.

We further stained the isolated protein bodies with ThT and visualized them under a confocal microscope using an Argon 458 nm laser. We observed strong ThT-positive signals (Fig. S4b, left panel) from the protein body isolates, which indicated the presence of amyloids. The unstained plant material was taken as a negative control (Fig. S4b, right panel). A limitation of these observations is that the isolated material may contain other proteins that could also exist as amyloids, and we could not confirm the identity of CRUs among them due to the unavailability of commercial antibodies against the protein. However, since CRU-3 is reported to be the most abundant protein among the SSPs of *Arabidopsis* [20,53], it is most likely that it contributes maximally to the obtained ThT signal.

4. Discussion

The SSPs have been implicated as a sustained source of nutrients during seed germination and are shown to form amyloid structures [8]. CRUs are the major SSPs in the Cruciferae plant family [19]. In this study, we used the LY12 peptide, inferred to be aggregation-prone by *in silico* APR prediction tools, as a surrogate for the CRU-3 isoform of the Cruciferin family of proteins. The LY12 peptide was found to form β-sheet rich amyloid fibrils *in vitro* and show characteristic ThT and CR positive signals. It follows nucleation-dependent aggregation kinetics similar to the canonical amyloidogenic peptides and proteins [54,55].

The finding that LY12 efficiently forms amyloids at neutral pH, while being inhibited at acidic conditions, presents a significant advantage. This suggests an industrial procedure for amyloid formation that is more akin to the physiological pathway, aligning with the protein's native environment in seeds, and offers a simplified method for fibrillation by avoiding harsh acidic treatments. This characteristic could broaden CRU-3's use in sustainable biomaterials and food products, potentially yielding unique amyloid structures. Nevertheless, it is important to acknowledge that these results stem from peptide studies, and comprehensive validation with the full-length CRU-3 protein is essential to verify its complete amyloidogenic profile.

The Proteinase K treatment of LY12 amyloid fibrils revealed a progressive yet incomplete degradation, highlighting their structural stability. Unlike pathological amyloids that often show extreme proteolytic resistance [43], LY12 fibrils exhibited a controlled and partial susceptibility. This balance likely arises from their unique architecture resolved by cryo-EM, in which a compact core is shielded by more accessible, low-density peptide layers. The steady decline in ThT fluorescence, culminating in a ~2.6-fold lower signal compared to untreated fibrils, together with TEM evidence of fibril fragmentation, suggests that proteinase action predominantly targets solvent-exposed peripheral regions while the cross β-core remains intact. This moderate resistance supports the hypothesis that SSP amyloids might have evolved as a trait to facilitate seed survival under challenging environmental conditions, while their partial susceptibility could facilitate mobilization during germination [56]. This stability is highly advantageous from the biomaterial and food application perspective. LY12 fibrils can maintain their structural integrity and functionality under physiological stress but are not entirely impervious to biological processing. This dual behavior not only alleviates concerns of uncontrolled persistence but also achieves a rare co-optimization of durability and biodegradability, positioning them as sustainable biocompatible scaffolds, controlled-release matrices, novel texturizing agents, and functional food formulations

with improved nutrient delivery.

The seeding capacity of LY12 fibrils that we observed can be capitalized to expedite amyloid formation, thereby facilitating and streamlining the industrial production of biomaterials. Similarly, the seeding potential of amyloids from several edible seeds, including cereals, pulses, hemp, and amaranth, which have been either isolated or studied *in vitro* to develop environment-friendly materials [12,41,57,58], should also be considered.

We present a high-resolution (2.86 Å) cryo-EM structure of LY12 fibrils, marking a significant revelation for plant-derived amyloids. An unusual structural feature of the LY12 fibrils is the presence of multiple peptide conformations. In stacks A and C, we found relatively straight peptide conformations, while stack B contained peptides that were kinked between residues A_{227} and L_{229}. This kinked structure is reminiscent of previously described conformations in certain peptide crystals, termed low-complexity amyloid-like reversible kinked segments (LARKS) [59]. LARKS have been implicated in contributing to the reversible nature of functional amyloid fibrils, *e.g.,* those from hnRNPA2 or FUS protein, as they are thought to introduce a thermodynamically unstable element into the fibril structure [60]. The observation of peptide conformations in LY12 fibrils that resemble these previously reported LARKS structures raises the possibility that LY12 fibrils are at least partially reversible.

Moreover, we noted the presence of extra density features at outer radial positions, suggesting that the dense fibril core is decorated with additional low-density peptide layers. As the extra density features were much weaker than the fibril core, it appears that the attached peptides are not present in every layer of the fibril and, thus, average out to a weaker density. This feature differentiates the observed LY12 fibrils from many pathological amyloid structures [61].

This study offers a comprehensive evaluation of the amyloidogenic potential of CRU-3 from *Arabidopsis thaliana*, focusing on its aggregation-prone LY12 peptide, and enhances our fundamental understanding of functional amyloids in the plant kingdom. It envisions to transform agricultural waste, specifically the de-oiled cake of *Arabidopsis*, into a sustainable alternative source of plant seed protein amyloids, having potential biomaterial and food industry applications.

However, future research is needed to elucidate the structure and dynamics of full-length CRU-3 amyloids *in vivo* to comprehensively reveal their physiological functions and biomaterial applications.

CRediT authorship contribution statement

Vijay Kumar: Conceptualization, Data curation, Formal analysis, Investigation, Methodology, Validation, Visualization, Writing – original draft, Writing – review & editing. **Nikolay Stoyanov:** Data curation, Formal analysis, Investigation, Methodology, Validation, Visualization, Writing – original draft, Writing – review & editing. **Vibha Kaushik:** Formal analysis, Visualization, Writing – original draft, Writing – review & editing. **Sourav Kumar:** Formal analysis, Visualization, Writing – review & editing. **Matthias Schmidt:** Resources, Supervision, Writing – review & editing. **Marcus Fändrich:** Funding acquisition, Resources, Supervision, Writing – review & editing. **Daniel Segal:** Conceptualization, Funding acquisition, Project administration, Resources, Supervision, Writing – original draft, Writing – review & editing.

Declaration of competing interest

The authors declare no conflict of interest.

Acknowledgments

We thank Lukas Kuhn (Ulm University, Germany) for technical support. Vijay Kumar and Sourav Kumar are recipients of the Tel Aviv University post-doctoral fellowship. Matthias Schmidt was supported by the Deutsche Forschungsgemeinschaft (Sonderforschungsbereich 1279/Z03 and A03). The collection of the cryo-EM datasets was supported by iNEXT Discovery (20842 and 24496), which were collected at the European Molecular Biology Laboratory, Heidelberg, Germany. These agencies had no role in study design, analysis and interpretation of data, writing of the report, and decision to submit the article for publication.

Appendix A. Supplementary data

Supplementary data to this article can be found online at https://doi.org/10.1016/j.ijbiomac.2026.151751.

Data availability

The reconstructed cryo-EM maps were deposited to the Electron Microscopy Data Bank with accession code EMD-53117. The coordinates of the fitted atomic models were deposited to the Protein Data Bank under the accession code 9QFM. Other data that support the findings of this study are available from the corresponding author upon reasonable request.

References

[1] K.E. Marshall, K.L. Morris, D. Charlton, N. O'Reilly, L. Lewis, H. Walden, L. C. Serpell, Hydrophobic, aromatic, and electrostatic interactions play a central role in amyloid fibril formation and stability, Biochemistry 50 (12) (2011) 2061–2071, https://doi.org/10.1021/bi101936c.

[2] D. Eisenberg, M. Jucker, The amyloid state of proteins in human diseases, Cell 148 (6) (2012) 1188–1203, https://doi.org/10.1016/j.cell.2012.02.022.

[3] F. Chiti, C.M. Dobson, Protein misfolding, functional amyloid, and human disease, Annu. Rev. Biochem. 75 (2006) 333–366, https://doi.org/10.1146/annurev.biochem.75.101304.123901.

[4] D.M. Fowler, A.V. Koulov, W.E. Balch, J.W. Kelly, Functional amyloid-from bacteria to humans, Trends Biochem. Sci. 32 (5) (2007) 217–224, https://doi.org/10.1016/j.tibs.2007.03.003.

[5] A. Surguchov, F.N. Emamzadeh, A.A. Surguchev, Amyloidosis and longevity: a lesson from plants, Biology 8 (2) (2019) 43, https://doi.org/10.3390/biology8020043.

[6] H. Mohammad-Beigi, L. Kjaer, H. Eskandari, F. Aliakbari, G. Christiansen, G. Ruvo, J.L. Ward, D.E. Otzen, A possible connection between plant longevity and the absence of protein fibrillation: basis for identifying aggregation inhibitors in plants, Front. Plant Sci. 10 (2019), https://doi.org/10.3389/fpls.2019.00148.

[7] K.S. Antonets, A.A. Nizhnikov, Predicting amyloidogenic proteins in the proteomes of plants, Int. J. Mol. Sci. 18 (10) (2017) 2155, https://doi.org/10.3390/ijms18102155.

[8] K.S. Antonets, M.V. Belousov, A.I. Sulatskaya, M.E. Belousova, A.O. Kosolapova, M. I. Sulatsky, E.A. Andreeva, P.A. Zykin, Y.V. Malovichko, O.Y. Shtark, A. N. Lykholay, K.V. Volkov, I.M. Kuznetsova, K.K. Turoverov, E.Y. Kochetkova, A. G. Bobylev, K.S. Usachev, O.N. Demidov, I.A. Tikhonovich, A.A. Nizhnikov, Accumulation of storage proteins in plant seeds is mediated by amyloid formation, PLoS Biol. 18 (7) (2020) e3000564, https://doi.org/10.1371/journal.pbio.3000564.

[9] N. Sinha, T. Zahra, A.Y. Gahane, B. Rout, A. Bhattacharya, S. Basu, A. Chakrabarti, A.K. Thakur, Protein reservoirs of seeds are amyloid composites employed differentially for germination and seedling emergence, Plant J. 116 (2) (2023) 329–346, https://doi.org/10.1111/tpj.16429.

[10] B. Liu, H. Zhang, X. Qin, Amyloid fibrils and their applications: current status and latest developments, Nanomaterials 15 (4) (2025) 255, https://doi.org/10.3390/nano15040255.

[11] Z. Wei, S. Dai, J. Huang, X. Hu, C. Ge, X. Zhang, K. Yang, P. Shao, P. Sun, N. Xiang, Soy protein amyloid fibril scaffold for cultivated meat application, ACS Appl. Mater. Interfaces 15 (12) (2023) 15108–15119, https://doi.org/10.1021/acsami.2c21702.

[12] T. Li, J. Zhou, M. Peydayesh, Y. Yao, M. Bagnani, I. Kutzli, Z. Chen, L. Wang, R. Mezzenga, Plant protein amyloid fibrils for multifunctional sustainable materials, Adv. Sustainable Syst. 7 (4) (2023) 2200414, https://doi.org/10.1002/adsu.202200414.

[13] D. Xu, J. Zhou, W.L. Soon, I. Kutzli, A. Molière, S. Diedrich, M. Radiom, S. Handschin, B. Li, L. Li, S.J. Sturla, C.Y. Ewald, R. Mezzenga, Food amyloid fibrils are safe nutrition ingredients based on in-vitro and in-vivo assessment, Nat. Commun. 14 (1) (2023) 6806, https://doi.org/10.1038/s41467-023-42486-x.

[14] T. Luyckx, C. Grootaert, M. Monge-Morera, J.A. Delcour, F. Rousseau, J. Schymkowitz, J. Van Camp, Bioavailability and health impact of ingested amyloid-like protein fibrils and their link with inflammatory status: a need for more research? Mol. Nutr. Food Res. 66 (9) (2022) 2101032 https://doi.org/10.1002/mnfr.202101032.

[15] Y. Liang, P. Zhang, M. Liu, H. Liu, B. He, Y. Zhu, J. Wang, Plant-based protein amyloid fibrils: origins, formation, extraction, applications, and safety, Food Chem. 469 (2025) 142559, https://doi.org/10.1016/j.foodchem.2024.142559.

[16] Y. Liu, L. Chen, S. Wu, P. Chen, Q. Jiang, W. Huang, Recent progress of plant protein-based amyloid-like nanofibrils, Food Hydrocoll. 160 (2025) 110749, https://doi.org/10.1016/j.foodhyd.2024.110749.
[17] R. Singh, S. Langyan, S. Sangwan, B. Rohtagi, A. Khandelwal, M. Shrivastava, Protein for human consumption from oilseed cakes: a review, Front. Sustain. Food Syst. 6 (2022), https://doi.org/10.3389/fsufs.2022.856401.
[18] A.E. Yaschenko, J.M. Alonso, A.N. Stepanova, *Arabidopsis* as a model for translational research, Plant Cell 37 (5) (2024), https://doi.org/10.1093/plcell/koae065.
[19] P.P. Pang, R.E. Pruitt, E.M. Meyerowitz, Molecular cloning, genomic organization, expression and evolution of 12S seed storage protein genes of *Arabidopsis thaliana*, Plant Mol. Biol. 11 (6) (1988) 805–820, https://doi.org/10.1007/BF00019521.
[20] T.-P. Nguyen, G. Cueff, D.D. Hegedus, L. Rajjou, L. Bentsink, A role for seed storage proteins in *Arabidopsis* seed longevity, J. Exp. Bot. 66 (20) (2015) 6399–6413, https://doi.org/10.1093/jxb/erv348.
[21] Y. Lin, A. Pajak, F. Marsolais, P. McCourt, C.D. Riggs, Characterization of a cruciferin deficient mutant of *Arabidopsis* and its utility for overexpression of foreign proteins in plants, PLoS One 8 (5) (2013) e64980, https://doi.org/10.1371/journal.pone.0064980.
[22] S. Chakrabortee, C. Kayatekin, G.A. Newby, M.L. Mendillo, A. Lancaster, S. Lindquist, Luminidependens (LD) is an *Arabidopsis* protein with prion behavior, Proc. Natl. Acad. Sci. USA 113 (21) (2016) 6065–6070, https://doi.org/10.1073/pnas.1604478113.
[23] A.C. Tsolis, N.C. Papandreou, V.A. Iconomidou, S.J. Hamodrakas, A consensus method for the prediction of 'aggregation-prone' peptides in globular proteins, PLoS One 8 (1) (2013) e54175, https://doi.org/10.1371/journal.pone.0054175.
[24] S.O. Garbuzynskiy, M.Y. Lobanov, O.V. Galzitskaya, Foldamyloid: a method of prediction of amyloidogenic regions from protein sequence, Bioinformatics 26 (3) (2009) 326–332, https://doi.org/10.1093/bioinformatics/btp691.
[25] M. Oliveberg, Waltz, an exciting new move in amyloid prediction, Nat. Methods 7 (3) (2010) 187–188, https://doi.org/10.1038/nmeth0310-187.
[26] S.H.W. Scheres, RELION: implementation of a Bayesian approach to cryo-EM structure determination, J. Struct. Biol. 180 (3) (2012) 519–530, https://doi.org/10.1016/j.jsb.2012.09.006.
[27] A. Rohou, N. Grigorieff, CTFFIND4: fast and accurate defocus estimation from electron micrographs, J. Struct. Biol. 192 (2) (2015) 216–221, https://doi.org/10.1016/j.jsb.2015.08.008.
[28] S.Q. Zheng, E. Palovcak, J.-P. Armache, K.A. Verba, Y. Cheng, D.A. Agard, MotionCor2: anisotropic correction of beam-induced motion for improved cryo-electron microscopy, Nat. Methods 14 (4) (2017) 331–332, https://doi.org/10.1038/nmeth.4193.
[29] D. Kimanius, K. Jamali, M.E. Wilkinson, S. Lövestam, V. Velazhahan, T. Nakane, S. H.W. Scheres, Data-driven regularisation lowers the size barrier of cryo-EM structure determination, bioRxiv (2023), https://doi.org/10.1101/2023.10.23.563586.
[30] A. Punjani, J.L. Rubinstein, D.J. Fleet, M.A. Brubaker, cryoSPARC: algorithms for rapid unsupervised cryo-EM structure determination, Nat. Methods 14 (3) (2017) 290–296, https://doi.org/10.1038/nmeth.4169.
[31] E.C. Meng, T.D. Goddard, E.F. Pettersen, G.S. Couch, Z.J. Pearson, J.H. Morris, T. E. Ferrin, UCSF ChimeraX: tools for structure building and analysis, Protein Sci. 32 (11) (2023) e4792, https://doi.org/10.1002/pro.4792.
[32] P. Emsley, B. Lohkamp, W.G. Scott, K. Cowtan, Features and development of *Coot*, Acta Crystallogr. D 66 (4) (2010) 486–501, https://doi.org/10.1107/S0907444910007493.
[33] W. Wriggers, R.A. Milligan, J.A. McCammon, Situs: a package for docking crystal structures into low-resolution maps from electron microscopy, J. Struct. Biol. 125 (2) (1999) 185–195, https://doi.org/10.1006/jsbi.1998.4080.
[34] D. Liebschner, P.V. Afonine, M.L. Baker, G. Bunkoczi, V.B. Chen, T.I. Croll, B. Hintze, L.-W. Hung, S. Jain, A.J. McCoy, N.W. Moriarty, R.D. Oeffner, B.K. Poon, M.G. Prisant, R.J. Read, J.S. Richardson, D.C. Richardson, M.D. Sammito, O. V. Sobolev, D.H. Stockwell, T.C. Terwilliger, A.G. Urzhumtsev, L.L. Videau, C. J. Williams, P.D. Adams, Macromolecular structure determination using X-rays, neutrons and electrons: recent developments in *Phenix*, Acta Crystallogr. D 75 (10) (2019) 861–877, https://doi.org/10.1107/S2059798319011471.
[35] T. Croll, ISOLDE: a physically realistic environment for model building into low-resolution electron-density maps, Acta Crystallogr. D 74 (6) (2018) 519–530, https://doi.org/10.1107/S2059798318002425.
[36] T. Nietzel, N.V. Dudkina, C. Haase, P. Denolf, D.A. Semchonok, E.J. Boekema, H.-P. Braun, S. Sunderhaus, The native structure and composition of the cruciferin complex in *Brassica napus*, J. Biol. Chem. 288 (4) (2013) 2238–2245, https://doi.org/10.1074/jbc.M112.356089.
[37] M. Biancalana, S. Koide, Molecular mechanism of Thioflavin-T binding to amyloid fibrils, Biochim. Biophys. Acta 1804 (7) (2010) 1405–1412, https://doi.org/10.1016/j.bbapap.2010.04.001.
[38] E.I. Yakupova, L.G. Bobyleva, I.M. Vikhlyantsev, A.G. Bobylev, Congo red and amyloids: history and relationship, Biosci. Rep. 39 (1) (2019), https://doi.org/10.1042/bsr20181415. BSR20181415.
[39] R. Kayed, J. Bernhagen, N. Greenfield, K. Sweimeh, H. Brunner, W. Voelter, A. Kapurniotu, Conformational transitions of islet amyloid polypeptide (IAPP) in amyloid formation *in vitro*, J. Mol. Biol. 287 (4) (1999) 781–796, https://doi.org/10.1006/jmbi.1999.2646.
[40] A. Tiiman, J. Krishtal, P. Palumaa, V. Tõugu, *In vitro* fibrillization of Alzheimer's amyloid-β peptide (1-42), AIP Adv. 5 (9) (2015) 092401, https://doi.org/10.1063/1.4921071.
[41] I. Kutzli, J. Zhou, T. Li, S.K. Baier, R. Mezzenga, Formation and characterization of plant-based amyloid fibrils from hemp seed protein, Food Hydrocoll. 137 (2023) 108307, https://doi.org/10.1016/j.foodhyd.2022.108307.
[42] A. Herneke, C. Lendel, D. Johansson, W. Newson, M. Hedenqvist, S. Karkehabadi, D. Jonsson, M. Langton, Protein nanofibrils for sustainable food–characterization and comparison of fibrils from a broad range of plant protein isolates, ACS Food Sci. Technol. 1 (5) (2021) 854–864, https://doi.org/10.1021/acsfoodscitech.1c00034.
[43] R.N. Rambaran, L.C. Serpell, Amyloid fibrils, Prion 2 (3) (2008) 112–117, https://doi.org/10.4161/pri.2.3.7488.
[44] A. Bansal, M. Schmidt, M. Rennegarbe, C. Haupt, F. Liberta, S. Stecher, I. Puscalau-Girtu, A. Biedermann, M. Fändrich, AA amyloid fibrils from diseased tissue are structurally different from *in vitro* formed SAA fibrils, Nat. Commun. 12 (1) (2021) 1013, https://doi.org/10.1038/s41467-021-21129-z.
[45] G. Andreotti, J. Baur, M. Ugrina, P.B. Pfeiffer, M. Hartmann, S. Wiese, H. Miyahara, K. Higuchi, N. Schwierz, M. Schmidt, M. Fändrich, Insights into the structural basis of amyloid resistance provided by cryo-EM structures of AApoAII amyloid fibrils, J. Mol. Biol. 436 (4) (2024) 168441, https://doi.org/10.1016/j.jmb.2024.168441.
[46] V.V. Kushnirov, A.A. Dergalev, A.I. Alexandrov, Proteinase K resistant cores of prions and amyloids, Prion 14 (1) (2020) 11–19, https://doi.org/10.1080/19336896.2019.1704612.
[47] P. Arosio, T.P.J. Knowles, S. Linse, On the lag phase in amyloid fibril formation, Phys. Chem. Chem. Phys. 17 (12) (2015) 7606–7618, https://doi.org/10.1039/C4CP05563B.
[48] S. Subedi, S. Sasidharan, N. Nag, P. Saudagar, T. Tripathi, Amyloid cross-seeding: mechanism, implication, and inhibition, Molecules 27 (6) (2022) 1776, https://doi.org/10.3390/molecules27061776.
[49] S. Mazzitelli, F. Filipello, M. Rasile, E. Lauranzano, C. Starvaggi-Cucuzza, M. Tamborini, D. Pozzi, I. Barajon, T. Giorgino, A. Natalello, M. Matteoli, Amyloid-β 1–24 C-terminal truncated fragment promotes amyloid-β 1–42 aggregate formation in the healthy brain, Acta Neuropathol. Commun. 4 (1) (2016) 110, https://doi.org/10.1186/s40478-016-0381-9.
[50] M.E. Oskarsson, J.F. Paulsson, S.W. Schultz, M. Ingelsson, P. Westermark, G. T. Westermark, *In vivo* seeding and cross-seeding of localized amyloidosis: a molecular link between type 2 diabetes and Alzheimer disease, Am. J. Pathol. 185 (3) (2015) 834–846, https://doi.org/10.1016/j.ajpath.2014.11.016.
[51] T. Heerde, A. Bansal, M. Schmidt, M. Fändrich, Cryo-EM structure of a catalytic amyloid fibril, Sci. Rep. 13 (1) (2023) 4070, https://doi.org/10.1038/s41598-023-30711-y.
[52] M. Kanai, M. Sugiyama, M. Kondo, K. Yamada, M. Nishimura, S. Mano, Fusing the 3'UTR of seed storage protein genes leads to massive recombinant protein accumulation in seeds, Sci. Rep. 13 (1) (2023) 12217, https://doi.org/10.1038/s41598-023-39356-3.
[53] L. Wan, A.R.S. Ross, J. Yang, D.D. Hegedus, A.R. Kermode, Phosphorylation of the 12 S globulin cruciferin in wild-type and *abi1-1* mutant *Arabidopsis thaliana* (Thale cress) seeds, Biochem. J. 404 (2) (2007) 247–256, https://doi.org/10.1042/bj20061569.
[54] F. Ferrone, Analysis of protein aggregation kinetics, in: R. Wetzel (Ed.), Methods in Enzymology, Academic Press, 1999, pp. 256–274.
[55] E. Chatani, N. Yamamoto, Recent progress on understanding the mechanisms of amyloid nucleation, Biophys. Rev. 10 (2) (2018) 527–534, https://doi.org/10.1007/s12551-017-0353-8.
[56] J. Santos, S. Ventura, Functional amyloids germinate in plants, Trends Plant Sci. 26 (1) (2021) 7–10, https://doi.org/10.1016/j.tplants.2020.10.001.
[57] S. Mykolenko, W.L. Soon, R. Mezzenga, Production and characterization of amaranth amyloid fibrils from food protein waste, Food Hydrocoll. 149 (2024) 109604, https://doi.org/10.1016/j.foodhyd.2023.109604.
[58] J. Zhou, T. Li, M. Peydayesh, M. Usuelli, V. Lutz-Bueno, J. Teng, L. Wang, R. Mezzenga, Oat plant amyloids for sustainable functional materials, Adv. Sci. 9 (4) (2022) 2104445, https://doi.org/10.1002/advs.202104445.
[59] M.P. Hughes, M.R. Sawaya, D.R. Boyer, L. Goldschmidt, J.A. Rodriguez, D. Cascio, L. Chong, T. Gonen, D.S. Eisenberg, Atomic structures of low-complexity protein segments reveal kinked β sheets that assemble networks, Science 359 (6376) (2018) 698–701, https://doi.org/10.1126/science.aan6398.
[60] M.P. Hughes, L. Goldschmidt, D.S. Eisenberg, Prevalence and species distribution of the low-complexity, amyloid-like, reversible, kinked segment structural motif in amyloid-like fibrils, J. Biol. Chem. 297 (4) (2021), https://doi.org/10.1016/j.jbc.2021.101194.
[61] T.W. Todd, N.N. Islam, C.N. Cook, T.R. Caulfield, L. Petrucelli, Cryo-EM structures of pathogenic fibrils and their impact on neurodegenerative disease research, Neuron 112 (14) (2024) 2269–2288, https://doi.org/10.1016/j.neuron.2024.05.012.